Geometric optimization of a rectangular isothermal block inside a lid-driven cavity by means of constructal design

GEOMETRIC OPTIMIZATION OF A RECTANGULAR ISOTHERMAL BLOCK INSIDE A LID-DRIVEN CAVITY BY MEANS OF CONSTRUCTAL DESIGN

Rafael da Silveira Borahel[1]; Flávia Schwarz Franceschini Zinani[1]; Luiz Alberto Oliveira Rocha[2-3], Elizaldo Domingues dos Santos[3], Liércio André Isoldi[4], Cesare Biserni[5]

[1]Mechanical Engineering Graduate Program, Universidade do Vale do Rio dos Sinos, 93022-750, São Leopoldo, Brazil
[2]Mechanical Engineering Graduate Program, Universidade Federal do Rio Grande do Sul, 90040-001, Porto Alegre, Brazil
[3]Computational Modeling Graduate Program, Universidade Federal do Rio Grande, 96203-900, Rio Grande, Brazil
[4]Graduate Program of Ocean Engineering, School of Engineering, Federal University of Rio Grande –FURG, Rio Grande, Italia Avenue, km 8, 96201-900, Brazil
[5]Department of Industrial Engineering (DIN), Alma Mater Studiorum - University of Bologna, Viale Risorgimento 2, 40136 Bologna, Italy

Abstract: The present work applies the Constructal Design method to analyze the performance of a rectangular isothermal block (IB) - inside an adiabatic lid-driven cavity with an isothermal lid - submitted to mixed convection heat transfer with unstable stratification. The effect of IB configuration on heat transfer performance is investigated via numerical simulation of heat and flow dynamics. The modeling for numerical simulations involves steady, laminar, and incompressible flow in a two-dimensional domain filled with a Newtonian fluid (air). Equations of mass, momentum, and energy balance are solved using numerical simulations based on the finite volume method (FVM). The main purpose of employing the Constructal Design method is to maximize the dimensionless heat transfer rate (q^*) between the IB and the surrounding fluid. The constraint are the cavity area and the IB/cavity area fraction (ϕ = 1/4, 1/8, 1/16, and 1/32), while the IB aspect ratio and its horizontal position are the degrees of freedom (DOF). The behavior of the system is investigated for different operational conditions given by the Richardson Number (Ri = 0.1, 1.0, and 10), for fixed Grashof ($Gr_{\sqrt{A}} = 10^5$) and Prandtl (Pr = 0.71) numbers. Considering all possible combinations of the analyzed parameters, 162 different geometric configurations were tested (54 for each Ri). The results indicate that higher heat transfer rates are associated with the largest aspect ratio tested for each IB-cavity area fraction. For ϕ = 1/16 and Ri = 0.1 – when the IB assumes a tall shape – q^* is 143.2% greater than the square shape. Considering all cases, the highest q^* is related to the flow dominated by forced convection (Ri = 0.1) and the IB placed to the right, where the IB-cavity area fraction and the IB aspect ratio are 1/4 and 3.0, respectively.

Keywords: Constructal Design. Lid-Driven Cavity. Laminar Flow. Mixed Convection Heat Transfer. Rectangular Obstacle.

NOMENCLATURE

A	Cavity Area	[m^2]
A_o	Isothermal Block Area	[m^2]
A_{q^*}	Heat Exchange Area	[m^2]
AR	Cavity Aspect Ratio	[–]
AR_o	Isothermal Block Aspect Ratio	[–]
C_p	Specific Heat	[$J.kg^{-1}.K^{-1}$]
$\vec{g}$	Gravity Acceleration	[$m.s^{-2}$]
$Gr_{\sqrt{A}}$	Grashof Number	[–]
H	Cavity Height	[m]
H^*	Dimensionless Cavity Height	[–]
H_o	Isothermal Block Height	[m]
$H_o{}^*$	Dimensionless Isothermal Block Height	[–]
k	Thermal Conductivity	[$W.m^{-1}.K^{-1}$]
L	Cavity Lenght	[m]
L^*	Dimensionless Cavity Lenght	[–]
L_c	Characteristic Lenght	[m]
L_o	Isothermal Block Lenght	[m]
$L_o{}^*$	Dimensionless Isothermal Block Length	[–]
$\overline{Nu}_{\sqrt{A_0}}$	Average Nusselt Number	[–]
p	Pressure	[Pa]
Pr	Prandtl Number	[–]
q	Heat Transfer Rate	[W]
q^*	Dimensionless Heat Transfer Rate	[–]
q''	Heat Flux	[$W.m^{-2}$]
$Re_{\sqrt{A}}$	Reynolds Number	[–]
Ri	Richardson Number	[–]
T	Temperature	[K]
T_{IB}	Isothermal Block Temperature	[K]
T_{lid}	Lid-driven Surface Temperature	[K]
T_r	Reference Temperature	[K]
u	Horizontal Velocity	[$m.s^{-1}$]
u^*	Dimensionless Horizontal Velocity	[–]

U_{lid}	Lid-driven Surface Velocity	[m.s^{-1}]
v	Vertical Velocity	[m.s^{-1}]
v^*	Dimensionless Vertical Velocity	[–]
W	Unitary Cavity Depth	[m]
x	Horizontal Cartesian Coordinates	[m]
x^*	Dimensionless Horizontal Cartesian Coordinates	[–]
x_o	Horizontal Position of the Isothermal Block Center	[m]
x_o^*	Dimensionless Horizontal Position of the Isothermal Block Center	[–]
y	Vertical Cartesian Coordinates	[m]
y^*	Dimensionless Vertical Cartesian Coordinates	[–]
y_o	Vertical Position of the Isothermal Block Center	[m]
y_o^*	Dimensionless Vertical Position of the Isothermal Block Center	[–]

Greek Symbols

β	Thermal Expansion Coefficient	[K^{-1}]
θ^*	Dimensionless Temperature	[–]
μ	Dynamic Viscosity	[kg.m^{-1}.s^{-1}]
ν	Kinematic Viscosity	[m^2.s^{-1}]
ρ	Density	[kg.m^{-3}]
ϕ	Area Fraction	[–]

1 INTRODUCTION

Life is a universal tendency in nature. It is a physical movement with the freedom to change. Every moving, flowing, and hurtling thing exhibits the tendency to move more easily and to keep moving by changing its configuration, path, and rhythm. This evolutionary flow organization and its end (death) are nature, the animate, and the inanimate realm together [1]. Human beings (and the engineered devices produced by them) are part of nature and governed by its laws, like the Constructal Law [2]. Constructal Law is a physical principle that affirms that a finite flow system, animate or inanimate, only persists in time (survives) if its configuration evolves to provide easier access to its internal streams (fluid, energy, species, etc.) [3–6]. This multidisciplinary law applies to "systems" of several areas, like building safety [7,8], economy [9], geoscience [10], medicine [11–14], sports [15], and urban planning [16,17]. In engineering, energy storage units [18–20], heat exchangers [21–24], and renewable energy systems [25–27] can be improved by employing the Constructal Theory, more specifically, the Constructal Design Method [28,29]. This method, based on constraints (geometrical or physical) and objectives (performance indicators), has been applied to achieve a better understanding of the influence of design over the performance in finite-size flow systems, aiming to maximize and/or minimize defined performance indicators [3,5]. A particular kind of system that can be improved by the Constructal Design Method is the lid-driven cavity subjected to convective flow, whose performance indicator is the heat transfer between the fluid flow and any surface inside the cavity with a different temperature.

Internal flow with heat transfer in lid-driven cavities is considered a classic engineering problem, mainly in the field of fluid dynamics [30–33]. Although this problem is computationally "simple," its physics is complex, involving the formation of main and secondary vortices, reattachment, and detachment of boundary layers [34]. Two different mechanisms simultaneously drive the heat transfer inside the cavity: forced convection (related to the shear flow produced by the lid-driven surface's movement) and natural convection (caused by the buoyancy flow generated by the temperature gradients) [35,36]. If both mechanisms have the same order of magnitude, it can be said that the heat transfer occurs by mixed convection [33,37–39]. The lid-driven cavity represents an idealization of the resulting flow inside a hole in a channel wall, flow between obstacles fixed at a channel wall, or even a space between fins. Such systems would be present in situations such as cooling of electronic components, as mentioned by Kareem *et al*. [40]

and studied by Nimmagadda *et al*. [41]. Due to this applicability, different studies about lid-driven cavities have been carried out over the last years in the literature [42], especially involving square cavities with heated obstacles inside.

Oztop *et al*. [43] studied this type of cavity and observed that a circular body inside the cavity could be used as a control parameter for heat transfer, fluid flow, and temperature distributions. For the mixed convection of air in a square cavity with an isothermal rotating cylinder inside, Khanafer and Aithal [44] verified that a higher clockwise rotational speed of the cylinder provided increases in the average Nusselt number ($\overline{Nu}$) for different Richardson numbers (*Ri*). Kareem and Gao [45] numerically investigated turbulent flow in a three-dimensional lid-driven cavity with a counterclockwise rotating cylinder. According to their results, $\overline{Nu}$ can be increased up to 93.3% (approximately) when the highest dimensionless rotational speed is tested. Similar observations are also made in other studies involving rotating cylinders [46,47], but for cavities filled by nanofluids in the presence of magnetic fields. For lid-driven cavities with triangular obstacles, Gangawane [48] explored the effects of Prandtl (*Pr*) and Grashof (*Gr*) numbers in a lid-driven cavity containing a triangular block with constant heat flux. The author observed some convective cells in the fluid flow when natural convection is dominant ($Gr \geq 10^3$), especially for lower *Pr* cases, where the size of these cells is expressive. Gangawane and Manikandan [49] also reported convective cells in the flow of a Newtonian fluid ($1 \leq Pr \leq 100$) inside a lid-driven cavity with a centered triangular body (isothermal or with constant heat flux). According to the authors, flow recirculations are observed due to fluid flow from heated triangular surfaces towards the vertical ambient wall.

Gangawane *et al*. [31] studied the effects of size and location of an isothermal triangular block in a top lid-driven cavity for various *Pr*, *Ri*, and *R*eynolds numbers (*Re*). The authors affirm that among the parameters tested, the size of the block is the one that most intensely affects the heat transfer and fluid flow. Conducting a similar study but using a triangular body with constant heat flux, Gangawane *et al*. [33] verified that the heat transfer could be maximized using high *Pr* fluids (oils) and larger triangular blocks centrally placed in the cavity. Manchanda and Gangawane [32] also verified the influence of the size of a triangular heated obstacle under the heat transfer of a non-Newtonian power-law fluid in a top lid-driven cavity. According to the authors, the highest $\overline{Nu}$ was obtained when the biggest triangular blocks were tested with $Ri = 10$ and $Re = 1000$. For rectangular obstacles, Islam *et al*. [30] analyzed how the size and location of a square heated block can affect the mixed convection in an adiabatic lid-driven cavity. For the

central block placement, their results indicated that larger square blocks could enhance $\bar{N}u$ when forced (Ri = 0.1) and mixed convection (Ri = 1.0) are dominant, while an opposite behavior (small blocks intensifying the heat transfer) was observed for the natural convection cases.

Morshed *et al*. [38] studied the laminar mixed convection flow in a square lid-driven cavity with two isothermal square bodies in different locations. For a fixed *Pr* (0.71) and a wide range of Reynolds number (100-500) and *Ri* (0.1-10), $\bar{N}u$ on the surfaces of the two bodies changed significantly with the placement location. According to the authors, when the square bodies are placed diagonally, they exhibit better heat transfer characteristics. Nasrin [50] investigated the aspect ratio role of a vertical lid-driven cavity – with a square heat conducting block inside - on the mixed magnetoconvective air flow with the Joule heating effect. For all *Ri* tested, the lowest aspect ratio (associated with a tall cavity) proved to be the most suitable for increasing the heat transfer. Recently, Alsabery *et al*. [51] examined the mixed convection of a two-phase hybrid nanofluid inside a wave lid-driven cavity with a non-heated-conducting square. The highest $\bar{N}u$ was obtained for two specific numbers (1 and 2) of undulations on the vertical active wave walls. Furthermore, increases in $\bar{N}u$ were also observed with higher *Ri* and volume fraction of hybrid nanoparticles. Jamshed *et al*. [52] also detected that $\bar{N}u$ is enhanced when the volume fraction of nanoparticles - in a vented-cavity with a heated elliptic cylinder inside – is higher. However, the highest $\bar{N}u$ are associated with the forced convection (low *Ri* values) cases, contrary to [51]. Hussain *et al*. [53] investigated the magneto-bioconvection flow of a hybrid nanofluid in a porous lid-driven cavity containing microorganisms. Based on their results, the authors state that the magnetic field can act as a key parameter on thermofluids and the heat transfer decreases with its increase. Recently, studies about mixed convection inside cavities still continue to generate interest, giving rise to publications such as Ahmed et *al.* [54], Alomari et *al.* [55], and Korei et *al.* [56].

Examples of studies involving mixed convection in lid-driven cavities motivated by the Constructal Design method can be found in Lorenzini et *al.* [57], Razera et *al*. [42], and Rodrigues et *al.* [36]. In these studies, the focus was to elucidate how the different geometric parameters of fins (rectangular [36,57] or semi-elliptic [42]) affect the heat transfer inside the cavity. Nonetheless, studies that apply the Constructal Design method to analyze the role of the geometric configuration of isothermal rectangular obstacles inside lid-driven cavities with mixed convection flow over the thermal performance and fluid dynamic and thermal behavior of fluid flow have not been seen in the literature,

mainly considering the variation of mixed convection conditions (represented here by the Richardson number). This work introduces a numerical analysis in which several geometrical and flow parameters are combined to improve the convective heat transfer in a square top lid-driven cavity filled with air (Pr = 0.71). The Constructal Design Method is applied to find the best geometry configuration using the isothermal block (IB) aspect ratio (0.5-10) and its horizontal position as the adopted Degrees of Freedom (DOF). The effect of the parameters Ri (0.1, 1.0, and 10) and the area fraction between IB and the cavity area (1/4, 1/8, 1/16, and 1/32) are also addressed.

2 PROBLEM DESCRIPTION

The thermal and flow behavior of a working fluid (air, Pr = 0.71) inside a lid-driven cavity, with an isothermal block submitted to mixed convection heat transfer with unstable stratification, are numerically investigated here. The schematic representation of the computational domain is shown in Figure 1:

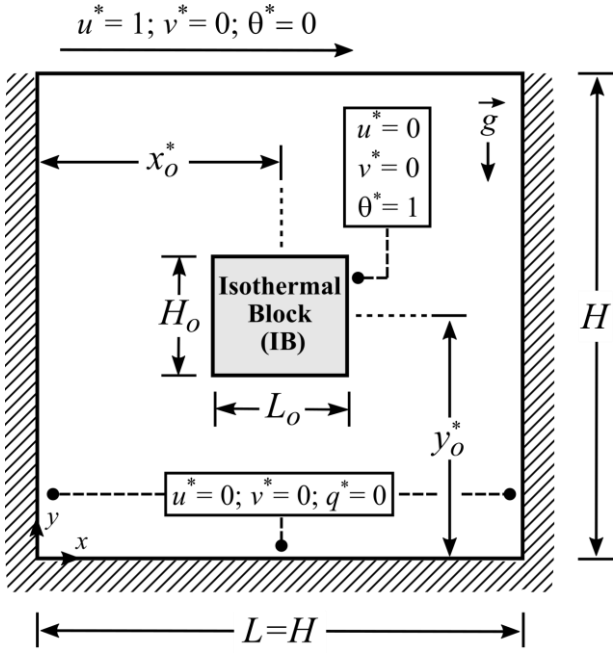

Figure 1 – Schematic Representation of the Computational Domain of lid-driven cavity mixed convection flow with internal isothermal rectangular block.

In order to maximize the heat transfer inside the cavity, the Constructal Design Method [3] is applied to achieve the best geometric configuration for the cavity, under distinct conditions. Figure 2 presents a flowchart that explains the method main steps, whose performance parameter is the dimensionless heat transfer rate (q^*), given by $q^* = (q/k.W.\Delta T)$, where q is the heat transfer rate at the IB walls, k is the thermal conductivity,

W is the unitary cavity depth and ΔT is the difference between the IB (T_{IB}) and lid-driven surface (T_{lid}) temperatures.

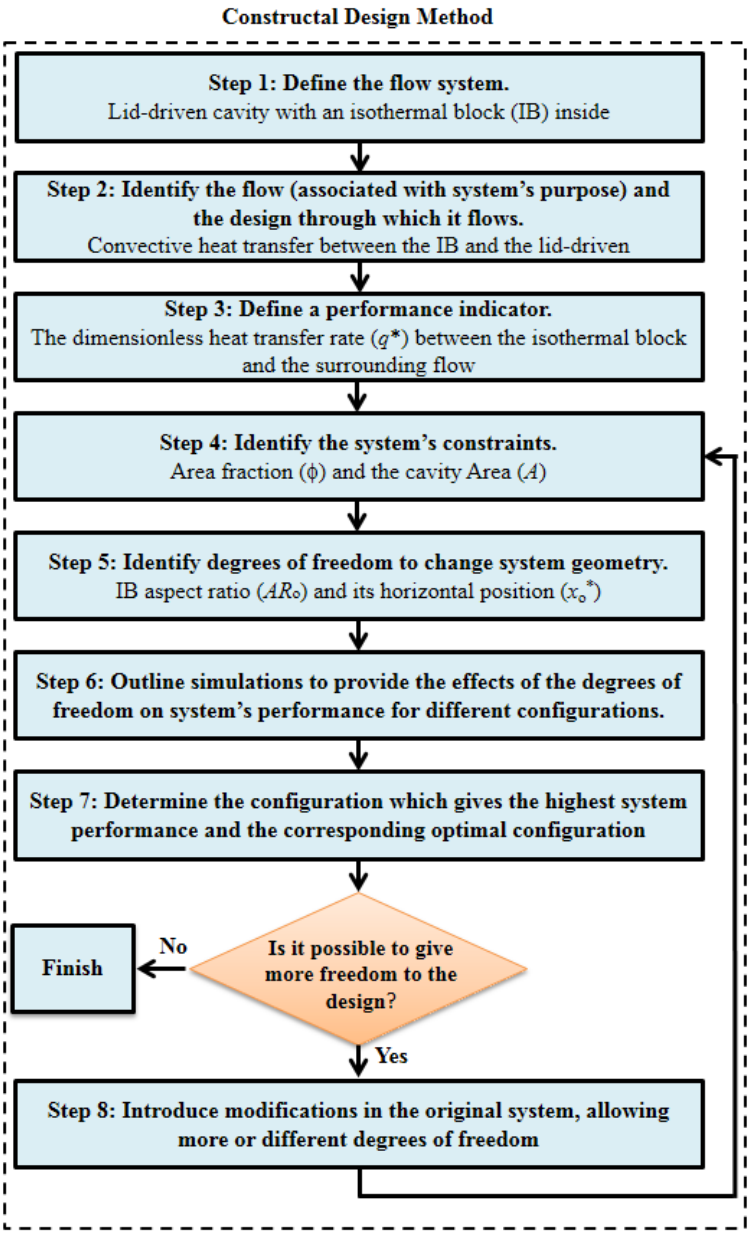

Figure 2 – Flowchart with the main steps of the Constructal Design Method applied in the present work.

To investigate how q^* can be affected by the flow and the isothermal block geometry, the IB aspect ratio ($AR_o = H_o / L_o$) and its horizontal position ($x_o^* = x_o / L$) are the degrees of freedom (DOF), where x_o is the horizontal position of the IB center. In addition, AR = H/L = 1 is also a degree of freedom kept constant in this work. The problem is subjected to two constraints, the areas of the cavity ($A = H \cdot L$) and isothermal block ($A_0 = H_0 \cdot L_0$), which are represented in their dimensionless form by $H^* \cdot L^* = 1$ and by the area fraction ($\phi = A_o / A$). Regarding the vertical position of the block ($y_o^* = y_o / H$),

it is kept constant ($y_o^* = 0.5$), since its effects on q^* are not analyzed here. Notice that $Gr_{\sqrt{A}}$ is the Grashof number and $Re_{\sqrt{A}}$ is the Reynolds number given by:

$$Gr_{\sqrt{A}} = \frac{\vec{g}\beta\Delta T(\sqrt{A})^3}{\nu^2} \tag{1}$$

$$Re_{\sqrt{A}} = \frac{U_{lid}\sqrt{A}}{\nu} \tag{2}$$

where $\vec{g}$ is the gravity acceleration, β is the thermal expansion coefficient, ν is the kinematic viscosity and U_{lid} is the lid velocity

Four ϕ values are tested in the present work: 1/4, 1/8, 1/16, and 1/32. For each ϕ, a different AR_o range are used, $0.5 \leq AR_o \leq 3.0$ ($\phi = 1/4$), $0.5 \leq AR_o \leq 6.0$ ($\phi = 1/8$ and 1/32) and $0.5 \leq AR_o \leq 10$ ($\phi = 1/16$). The AR_o limits are stipulated to prevent an IB extremely thin or a too-small space between the IB and the cavity walls, guaranteeing that under no circumstances H_o and L_o are less than 5% or exceed 90% of H and L. A fixed value (10^5) is used to $Gr_{\sqrt{A}}$, while $Re_{\sqrt{A}}$ is varied to obtain Ri = 0.1, 1.0, and 10 (forced, mixed, and natural convection), given by $Ri = Gr_{\sqrt{A}}/\left(Re_{\sqrt{A}}\right)^2$. Considering all geometric parameters analyzed, 162 different configurations were tested (54 for each Ri) for the lid-driven cavity.

2.2 Mathematical Model

The mathematical model is based on the balance equations of mass, momentum (in x and y directions), and energy (see Bejan [58]), respectively described by Eqs. (3-6). The simplifying hypothesis of Newtonian fluid, two-dimensional, laminar, incompressible, and steady-state flow are considered. The Boussinesq approximation is used to model buoyancy due to temperature variations, and thermophysical properties are kept constant.

$$\frac{\partial u}{\partial x} + \frac{\partial v}{\partial y} = 0 \tag{3}$$

$$\rho\left(u\frac{\partial u}{\partial x} + v\frac{\partial u}{\partial y}\right) = -\frac{\partial p}{\partial x} + \mu\left(\frac{\partial^2 u}{\partial x^2} + \frac{\partial^2 u}{\partial y^2}\right) \tag{4}$$

$$\rho\left(u\frac{\partial v}{\partial x}+v\frac{\partial v}{\partial y}\right)=-\frac{\partial p}{\partial y}+\mu\left(\frac{\partial^2 v}{\partial x^2}+\frac{\partial^2 v}{\partial y^2}\right)+\rho\vec{g}\beta(T-T_r) \tag{5}$$

$$\rho C_p\left(u\frac{\partial T}{\partial x}+v\frac{\partial T}{\partial y}\right)=k\left(\frac{\partial^2 T}{\partial x^2}+\frac{\partial^2 T}{\partial y^2}\right) \tag{6}$$

where x and y are the cartesian coordinates in the horizontal and vertical directions, u and v are the flow velocities in the horizontal and vertical directions, p is the pressure, μ is the dynamic viscosity, ρ is the density, Cp is the specific heat, T is the fluid temperature, and T_r is the reference temperature that is equal to T_{lid}.

The dimensionless forms of the geometric and flow parameter, i.e., Cartesian coordinates (x and y), cavity (H and L), and IB (H_o and L_o) dimensions, are defined as follows:

$$x^*, y^*, H^*, L^*, H_o^*, L_o^* = \frac{x, y, H, L, H_o, L_o}{\sqrt{A}} \tag{7}$$

$$u^*, v^* = \frac{u, v}{U_{lid}} \tag{8}$$

$$\theta^* = \frac{T - T_{lid}}{T_{IB} - T_{lid}} \tag{9}$$

$$p^* = p/\rho U_{lid}^2 \tag{10}$$

where x^* and y^* are the dimensionless Cartesian coordinates, u^* and v^* are the dimensionless velocity components, θ^* is the dimensionless temperature and p^* is the dimensionless pressure.

Thus, applying Eqs. (7-9) and the Pr (given by $Cp.\mu/k$), Re and Ri definitions, the balance equations [Eqs. (3-6)] take the following form:

$$\frac{\partial u^*}{\partial x^*}+\frac{\partial v^*}{\partial y^*}=0 \tag{10}$$

$$u^* \frac{\partial u^*}{\partial x^*} + v^* \frac{\partial u^*}{\partial y^*} = -\frac{\partial p^*}{\partial x^*} + \frac{1}{Re}\left(\frac{\partial^2 u^*}{\partial (x^*)^2} + \frac{\partial^2 u^*}{\partial (y^*)^2}\right) \quad (11)$$

$$u^* \frac{\partial v^*}{\partial x^*} + v^* \frac{\partial v^*}{\partial y^*} = -\frac{\partial p^*}{\partial y} + \frac{1}{Re}\left(\frac{\partial^2 v^*}{\partial (x^*)^2} + \frac{\partial^2 v^*}{\partial (y^*)^2}\right) + Ri.\theta^* \quad (12)$$

$$u^* \frac{\partial \theta^*}{\partial x^*} + v^* \frac{\partial \theta^*}{\partial y^*} = \frac{1}{RePr}\left(\frac{\partial^2 \theta^*}{\partial (x^*)^2} + \frac{\partial^2 \theta^*}{\partial (y^*)^2}\right) \quad (13)$$

2.2.1 Boundary Conditions

As illustrated in Fig 1, the non-slip condition ($u^* = v^* = 0$) is applied to all stationary walls of the cavity and IB, while a constant rightward velocity ($u^* = 1$) is prescribed to the lid wall. The adiabatic condition ($q^* = 0$) is considered in the bottom, left, and right cavity walls, the lowest temperature ($\theta^* = 0$) is adopted in the lid-driven surface and the highest temperature ($\theta^* = 1$) in the IB walls.

2.3 Numerical Model

In the present study, all numerical simulations are performed using the commercial software ANSYS Fluent 2021 R1, which employs the finite volume method (FVM) to solve Eqs. (3) – (6). The solver is pressure-based and different algorithms are employed to solve the problem. The SIMPLE algorithm is adopted for the pressure-velocity coupling, PRESTO! for the pressure interpolation, *Least Squares Cell-Based* for the gradient discretization, and *Second-Order Upwind* for the advective terms of momentum and energy equations. A residual of 10^{-6} is adopted as convergence criteria of the conservative equations of mass and momentum, while 10^{-8} is assumed to the energy.

2.3.1 Mesh Quality Analysis

Structured grid meshes, made of quadrilateral cells, are used in the spatial discretization of the computational domain. Close to the cavity and IB walls, more cells are used, configuring a refinement in the regions where the largest velocity and temperature gradients occur. The mesh quality analysis employs the GCI (*Grid Convergence Index*) method [59,60]. Applying the method, three grid meshes with different quantities of cells (66.858; 39.640 and 23.620 cells) - respectively named M1,

M2, and M3 – are tested in the computational domain for a critical case (ϕ = 1/4, AR_o = 2.0 and Ri = 10). The proposed analysis considers three control parameters: v^*_{min} and v^*_{max} at H^* = 0.5 and q^*. For v^*_{min}, the numerical uncertainty between M1 and M2 (GCI_{21}) and M2 and M3 (GCI_{32}) are, respectively, 0.32 % and 0.15 %. For the other variables, GCI_{21} and GCI_{32} are 0.05 % and 0.009 % for v^*_{max} and 0.007 % and 0.02 % for q^*. Thus, grounded in the GCI method, the M1 mesh (shown in Fig. 3) proves to be adequate for the spatial discretization so that all the other meshes are based on it.

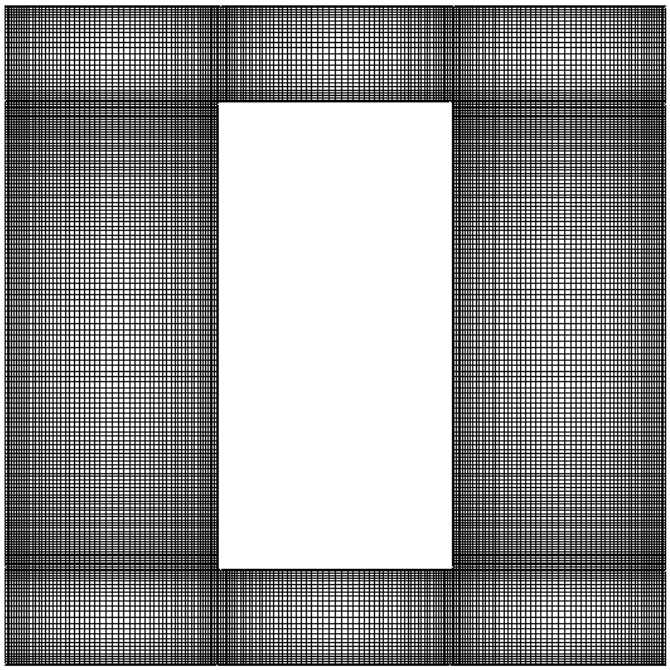

Figure 3 – Grid mesh for cavity with ϕ = 1/4 and AR_o = 2.0.

2.3.2 Model Verification

In order to verify the mathematical and numerical model, the studies of Islam *et al.*[30] and Moraga *et al.* [61] were reproduced. In these studies, a lid-driven cavity, with low temperatures prescribed in the walls and a square isothermal block inside, are analyzed for Ri = 0.1; 1.0 and 10. For these cavities, Fig. 4 (a-c) shows the u^* and v^* profiles, at L^* = 0.5 and H^* = 0.5, from Islam *et al.* [30], Moraga *et al.* [61] and the obtained in the present work. The results are quite similar, mainly for Ri = 0.1 and 1.0 [Fig. 4 (a-b)]. For Ri = 10 [Fig. 4 (c)], some differences are observed for u^*, when $0.6 \leq y^* \leq 0.9$. The convergence criteria can explain these differences. While Islam *et al.*[30] used 10^{-5}, 10^{-5}, and 10^{-6} for the conservative equations of mass, momentum and energy, this work used the values of 10^{-6}, 10^{-6}, and 10^{-8}. Despite these differences, the results obtained are still very similar to Moraga *et al.* [61], proving that the model can

satisfactorily reproduce, the u^* and v^* profiles.

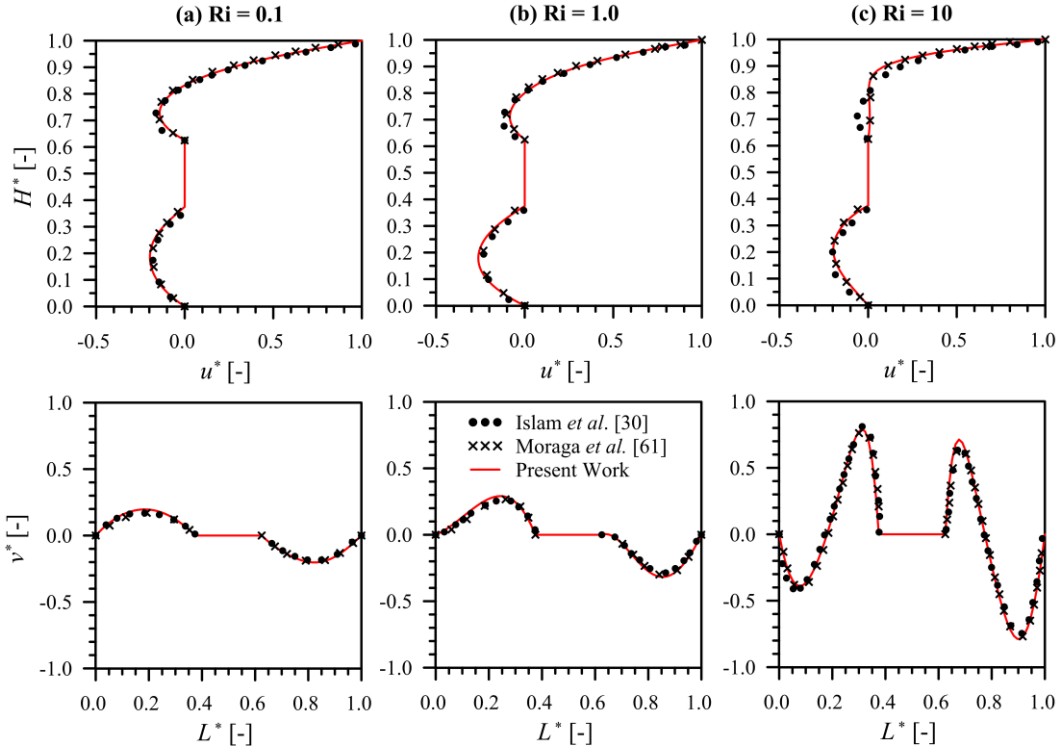

Figure 4 – u^* and v^* profiles, at L^* = 0.5 and H^* = 0.5, from Islam *et al*. [30], Moraga *et al*. [61] and Present Work, for (a) *Ri* = 0.1, (b) 1.0 and (c) 10.

Table 2 presents the average Nusselt number ($\bar{N}u$) at IB surfaces, obtained by Islam *et al*. [30] and presented work, using $\bar{N}u_{\sqrt{A_o}} = (q''.\sqrt{A_o}) / (k.\Delta T)$; where q'' is the heat flux at IB surfaces and A_o is the block area. For all the *Ri* tested, $\bar{N}u_{\sqrt{A_o}}$ proved to be very similar to those reported by Islam *et al*.[30]. The largest percentage difference ($\Delta\bar{N}u_{\sqrt{A_o}}$) is 1.78 % (*Ri* = 1.0); while for *Ri* = 0.1 and 10, $\Delta\bar{N}u$ are 0.18 % and 0.12 %, respectively. Thus, considering $\bar{N}u_{\sqrt{A_o}}$ and u^* and v^* profiles, it can be said that the implemented model is adequate for the proposed study.

Table 2 – $\bar{N}u_{\sqrt{A_o}}$ from Islam *et al*. [30] and Present Work, for *Ri* = 0.1, 1.0, and 10.

$\bar{N}u_{\sqrt{A_o}}$ [-]	***Ri* = 0.1**	***Ri* = 1.0**	***Ri* = 10**
Islam *et al*. [30]	5.57	5.70	7.98
Present Work	5.56	5.60	7.97
$\Delta\bar{N}u_{\sqrt{A_o}}$ [%]	0.18	1.78	0.12

3 RESULTS AND DISCUSSIONS

In this section, all results are presented in the dimensionless form. The first investigation concerns the flow features inside the cavity. The ease to flow is a condition to improve heat transfer. Fig. 5 shows u^* profiles along the vertical mid-plane ($L^* = 0.5$) for different AR_o, ϕ, and Ri.

As expected, the highest u^* are reported on the lid surface ($L^* = 1$), while some velocity peaks of similar magnitude ($u^* \approx 1$), but in the negative direction, are noticed in the region between the IB and the bottom cavity wall when $Ri = 10$. These peaks, observed in Fig. 5 (c) for $AR_o = 2.0$ ($\phi = 1/4$), 4.0 ($\phi = 1/8$) and 9.0 ($\phi = 1/16$), can be related to the space that the fluid has to flow in this region. Although the different AR_o and ϕ values, the bottom channel width is approximately the same ($0.15H^*$), proving the importance of this geometric parameter for the flow. In the upper cavity regions, when $Ri = 10$ and $\phi = 1/32$ [Fig. 5 (c) (iv)], inflections in u^* profiles can be observed for all AR_o analyzed. This behavior indicates changes in the flow direction, suggesting the existence of recirculation. Milder relevant flow recirculation in the upper cavity channel are also noted for the $\phi = 1/4$ cases, but only when $AR_o = 0.5$ are tested [Fig. 5 (a-c) (i)], showing that the highest occupation of the block into the cavity led to smoothing of the recirculation flow in the upper region of the cavity. Especially in these cases, Ri proved to be irrelevant to the occurrence of flow recirculation once this behavior is observed for all Ri. In spite of that, a comparison between the same configurations and fraction area of the isothermal block indicated that the velocity profiles (and the dynamic of the fluid flow) are changed by the Richardson number of the fluid flow. For instance, when $AR_o = 0.5$ and $\phi = 1/4$, the intensity of recirculation in the upper region of the cavity is intensified with the augmentation of the magnitude of Ri.

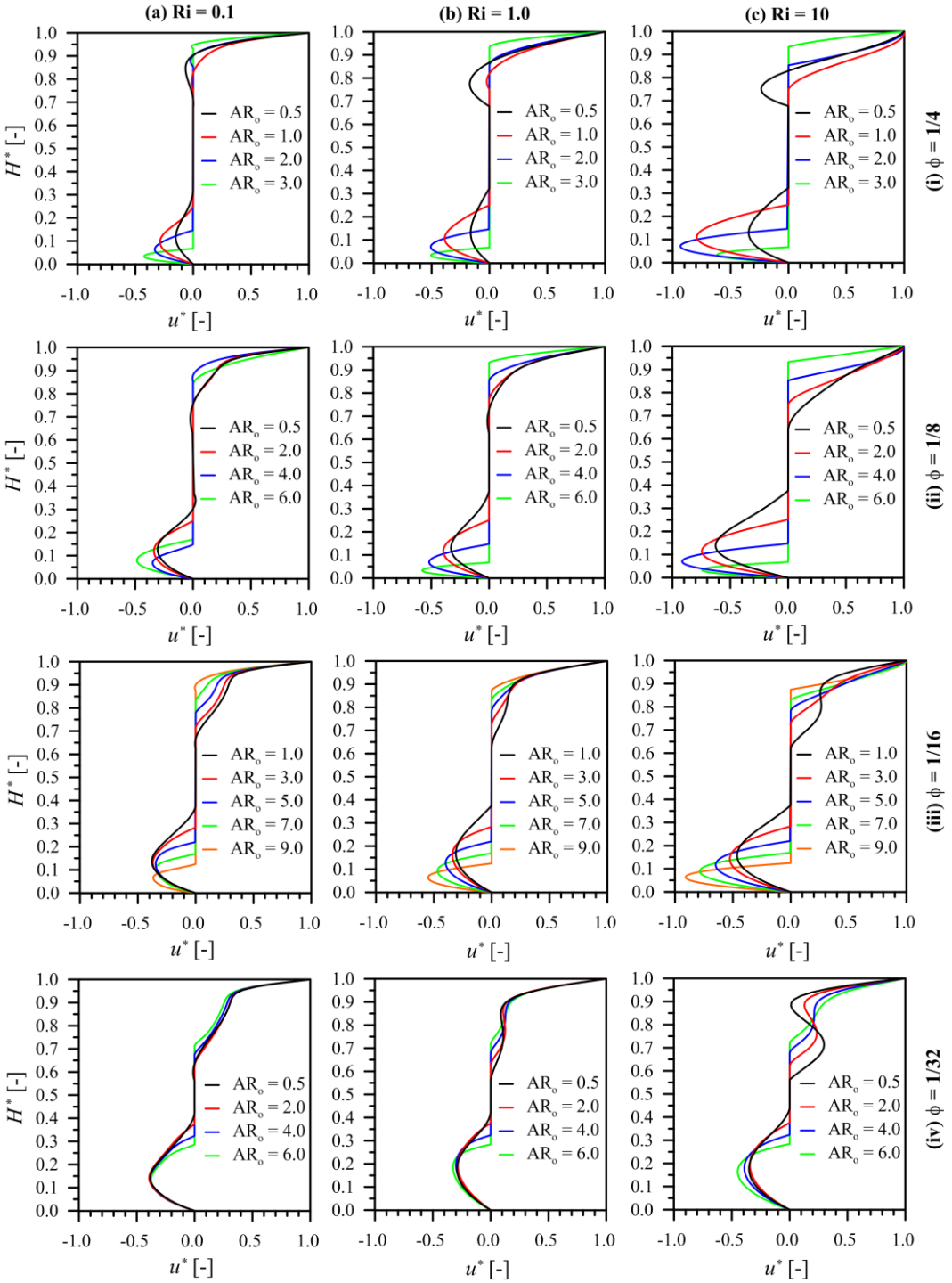

Figure 5 – u^* profiles along the vertical mid-plane (L^* = 0.5) for different AR_o, where: (a) Ri = 0.1, (b) Ri = 1.0, (c) Ri = 10 and (i) ϕ = 1/4, (ii) ϕ = 1/8, (iii) ϕ = 1/16, (iv) ϕ = 1/32.

The v^* profiles along the horizontal mid-plane (H^* = 0.5) for different AR_o, ϕ, and Ri are presented in Fig. 6. As can be seen, the highest v^* are noticed when Ri = 10 is used [Fig. 6 (c)]. For these cases, regardless of the ϕ employed, negative v^* peaks of great magnitude are observed close to the right cavity wall. The difference between the magnitudes of velocity in the right and left side of the isothermal block is also caused by the imposed flow of lid-driven surface, which increases the momentum intensity in the

downstream surface region of the cavity. For ϕ = 1/8, 1/16, and 1/32, negative $v^*_{\max}$ greater than -1.0 are registered for some $AR_{o,}$ which indicates that the negative *v* modulus is greater than U_{lid}. The natural convection, generated by the higher buoyancy forces when *Ri* = 10, can explain this behavior of the flow. In addition to the negative v^* peaks already reported, positive v^* peaks can also be observed in Fig. 6 (c) close to the IB right surface. These peaks exert a contrary movement to the main flow that occurs in the negative direction, suggesting the existence of vortex cells in the right cavity channel, which possibly accelerate the flow, thus explaining the greater negative $v^*_{\max}$ related to the cases with *Ri* = 10. Although indications of the existence of the vortex cells are also observed for the other *Ri* [Fig. 6 (a-b)], the flow is not affected in the same way since the buoyancy forces are smaller because the natural convection is not dominant. In general, on the right channel of the cavity, the positive magnitudes of v^* are associated with the natural convection mechanism generating an ascending plume close to the IB, while the flow imposed by the sliding wall causes a downward flow generating a layer shear with the rising plume. As *Ri* increases, this process is intensified, so there is a marked variation in the velocity fields of the cases of higher *Ri*.

The features of these convective cells inside the cavity can be observed in Fig. 7, where the velocity vectors of the highest AR_o (3.0, 6.0, 10, and 6.0) are presented for each ϕ (1/4, 1/8, 1/16, and 1/32) and *Ri* (0.1, 1.0 and 10) tested.

As can be seen, convective cells are noticed in the right cavity region for practically all cases, except ϕ = 1/32 (AR_o = 6.0) for *Ri* = 0.1 [Fig. 7 (a) (iv)], which presents a different flow pattern. For ϕ = 1/4 (AR_o = 3.0) and 1/8 (AR_o = 6.0), the right convective cell takes an elongated shape as *Ri* increases, occupying the entire right cavity channel [Fig. 7 (c) (i-ii)]. Flow changes in the left cavity region were also observed with the *Ri* increasing. For all ϕ analyzed, an upward flow, close to the left cavity wall, is observed when *Ri* = 0.1 is adopted [Fig. 7 (a) (i-iv)]. However, this upward flow occurs close to the IB left surface when *Ri* increases, even forming a counterclockwise convective cell for *Ri* = 10 and ϕ = 1/8, 1/16, and 1/32 [Fig. 7 (c) (ii-iv)]. Certainly, these distinct flow characteristics can affect the heat transfer inside the cavity.

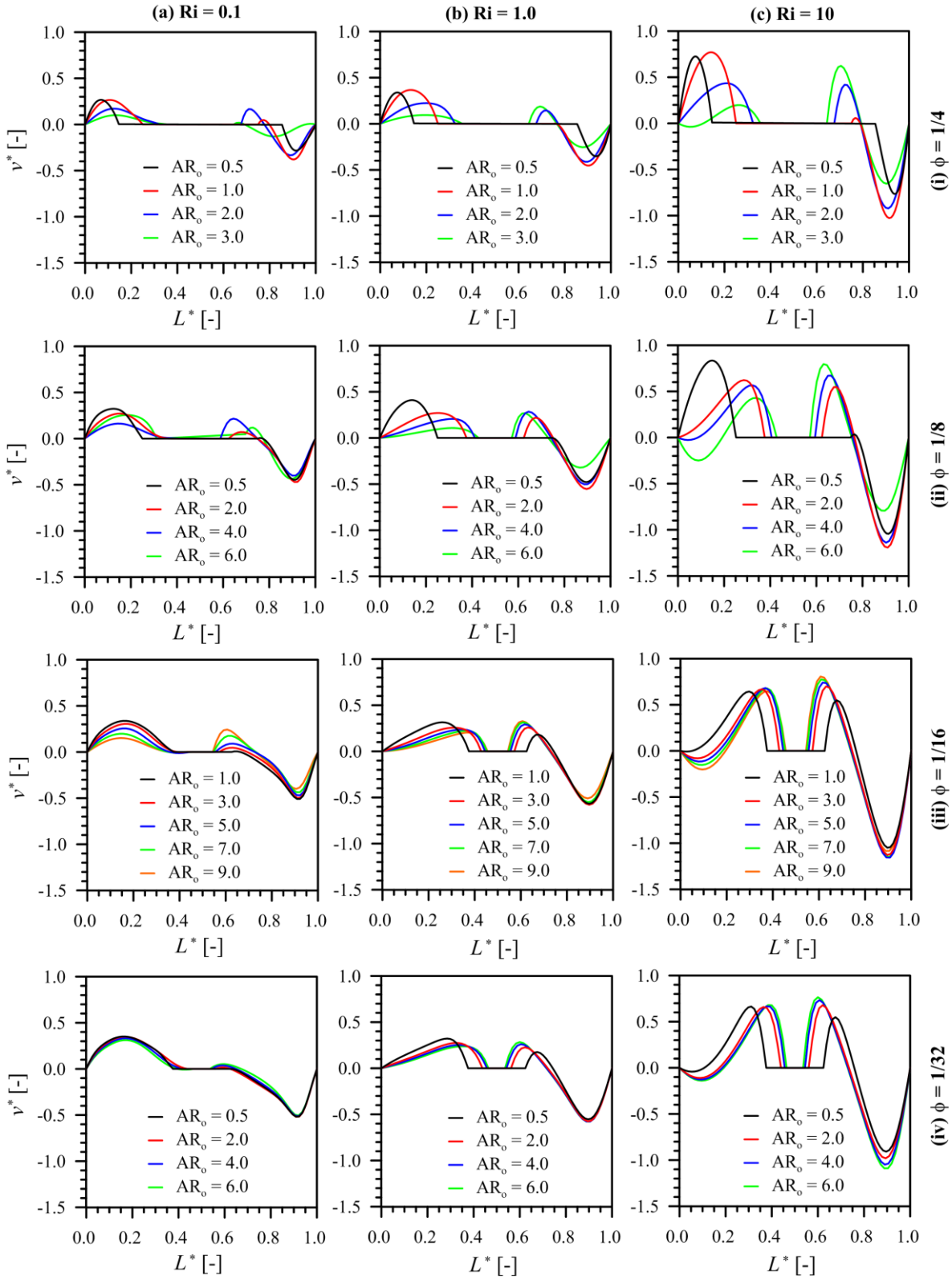

Figure 6 – v^* profiles along the horizontal mid-plane ($H^* = 0.5$) for different AR_o, where: (a) Ri = 0.1, (b) Ri = 1.0, (c) Ri = 10 and (i) ϕ = 1/4, (ii) ϕ = 1/8, (iii) ϕ = 1/16, (iv) ϕ = 1/32.

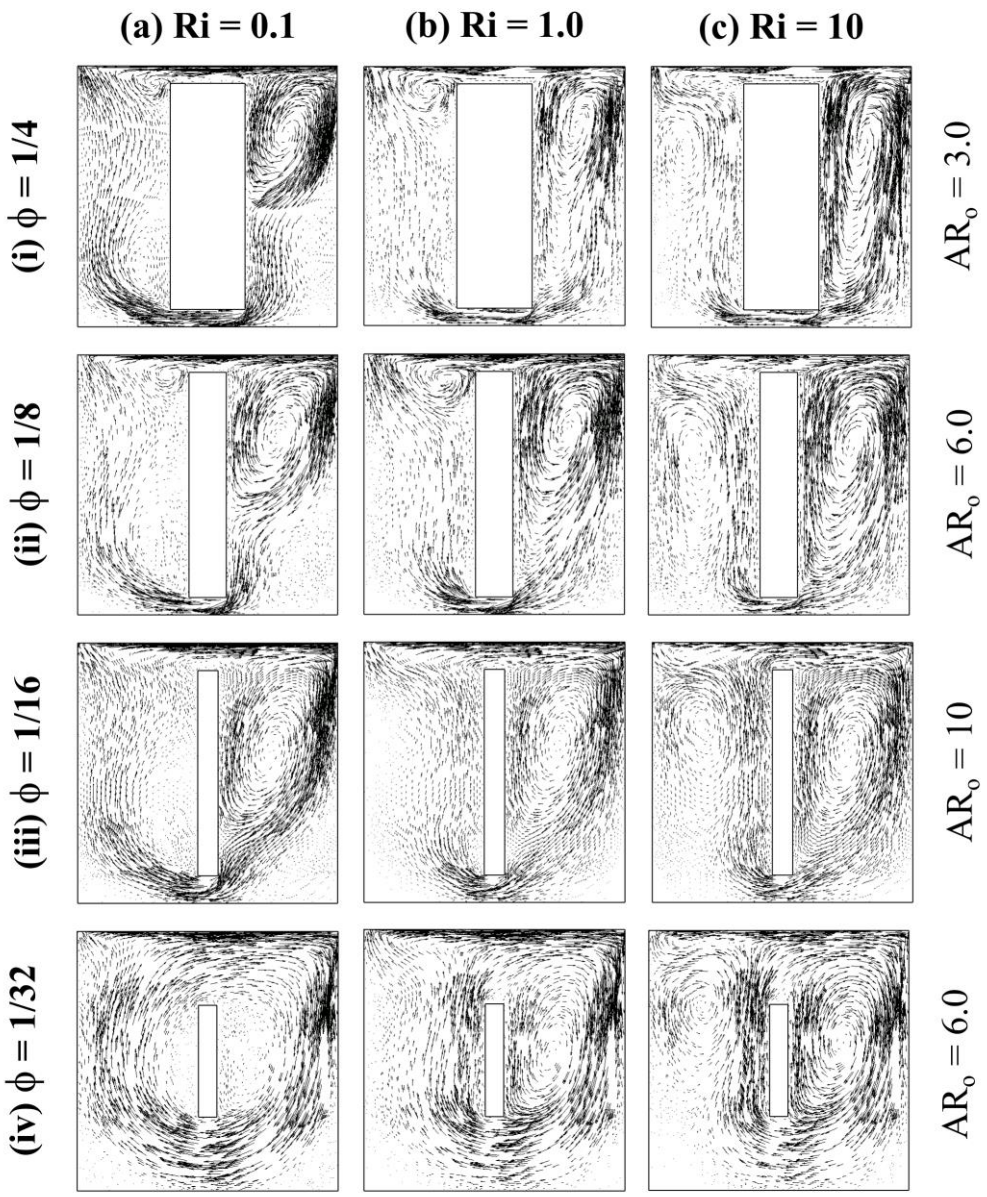

Figure 7 –Velocity vectors for the highest AR_o tested for each ϕ and Ri, where: (a) Ri = 0.1, (b) Ri = 1.0, (c) Ri = 10 and (i) ϕ = 1/4, (ii) ϕ = 1/8, (iii) ϕ = 1/16, (iv) ϕ = 1/32.

The AR_o and Ri effects on the dimensionless heat rate (q^*) are presented in Fig. 8 for (a) ϕ = 1/4, (b) 1/8, (c) 1/16, and (d) 1/32. Schematics of some cavities also are included in the figure, making the results easier to understand.

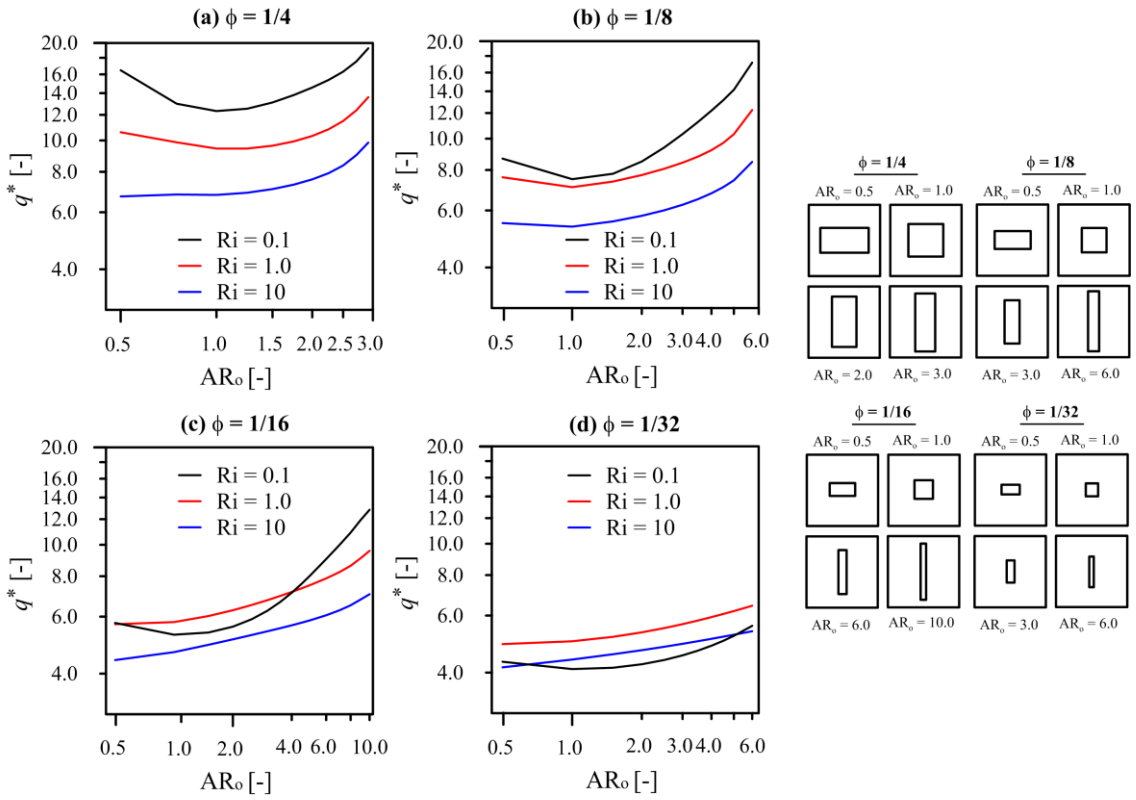

Figure 8 – HB aspect ratio (AR_o) and Ri effects on the dimensionless heat transfer rate (q^*) for (a) ϕ = 1/4, (b) ϕ = 1/8, (c) ϕ = 1/16 and (d) ϕ = 1/32.

As can be seen, the highest q^* are associated with the largest AR_o tested for each ϕ, regardless of Ri. For ϕ = 1/8 and Ri = 0.1 [Fig. 8 (b)], q^* is 129.1% greater when AR_o increases from 1.0 to 6.0. In the same figure, but for Ri = 1.0 and Ri = 10, q^* increases 73.1% and 58.5%, respectively, if the same AR_o variation are adopted. Considering all cases, the most pronounced increase in q^* (143.2% greater) is observed for ϕ = 1/16 and Ri = 0.1 [Fig. 8 (c)] when the IB assumes a tall shape (AR_o = 10) instead of the square shape (AR_o = 1.0). These variations in q^* can be explained by the IB perimeter that increases with AR_o, affecting the heat exchange area when AR_o > 1.0. Although A_o is constant for the same ϕ, the heat exchange area (A_{q^*}) varies as a perimeter function. Therefore, A_{q^*} is larger for the highest AR_o cases, enhancing the heat transfer inside the cavity. In addition to AR_o, q^* is also affected by the Richardson number, as well as, other factors that plays an important role in the convective heat transfer coefficient. For ϕ = 1/4 and 1/8 [Fig. 8 (a-b)], q^* is greater for all AR_o using Ri = 0.1, followed by Ri = 1.0 and 10. In the present work, the greatest q^* (19.2) is related to Ri = 0.1 for ϕ = 1/4 and AR_o = 3.0, while for the same geometry q^* is equal 13.6 for Ri = 1.0 and 9.8 for Ri = 10. In percentage numbers, q^*_{max} for Ri = 0.1 is 41.5% greater than Ri = 1.0 and 95.6% if compared to Ri = 10. Different behavior between q^* and Ri is observed to ϕ = 1/16 [Fig. 8 (c)], where the highest q^* are associated to Ri = 0.1 only for AR_o > 4.0. Furthermore, Ri

= 1.0 provides a more intense heat transfer when $\phi = 1/32$ [Fig. 8 (d)]. These contradictory behaviors are better understood when Fig. 8 is analyzed in conjunction with the Fig. 9.

Fig. 9 shows the θ^* fields and the velocity vectors when $AR_o = 2.0$ and 6.0 are tested for Ri = (a) 0.1 and (b) 1.0 and ϕ = (i) 1/16 and (ii) 1/32. In the right region of the cavity, relevant convective cells, for both AR_o and ϕ, can be observed when Ri = 1.0 (mixed convection) are adopted. However, these convective cells are not noticed when Ri = 0.1 (forced convection), which can explain the different behavior observed for q^* [Fig. 8 (c-d)] when ϕ = 1/16 and 1/32. For ϕ = 1/32, due to the small size of the IB, the blockage imposed on the flow is practically irrelevant, not affecting the flow. In these cases, any recirculation is due solely to the fluid buoyancy forces induced by density and temperature changes. As in the forced convection, the buoyancy forces do not prevail, and the recirculation will not arise unless the flow is affected by the IB geometry, which does not occur for $\phi = 1/32$. For this reason, the flow occurs close to the cavity walls for $\phi = 1/32$ and Ri = 0.1, which results in an unsatisfactory cooling of the IB, as suggested by the smallest q^* in Fig. 8 (d) and the more pronounced heating of the flow only close to the IB in Fig. 9 (a) (i-ii).

The θ^* fields and the velocity vectors for $\phi = 1/4$ are presented in Fig. 10 for AR_o = 1.0, 2.0 and 3.0 and Ri = 0.1, 1.0 and 10. For Ri = 0.1 [Fig. 10 (a)], relevant recirculations are observed in the right cavity region when AR_o = 2.0 and 3.0, which does not occur for ϕ = 1/32 [Fig. 9 (a)]. This behavior confirms that recirculations can be caused by the blockage imposed on the flow by large IBs of tall shape. Due to these recirculations, a portion of the fluid returns to the top of the cavity, where it is cooled. It explains why the right side of the cavity heats up gently for all Ri [Fig. 10 (a-c)]. Briefly, two factors explain the greatest q^* observed in Fig. 8 for the $\phi = 1/4$ cases: the existence of relevant circulations in the flow and the heat exchange area that increases with the IB size, the last one also observed for triangular [31,33] isothermal blocks.

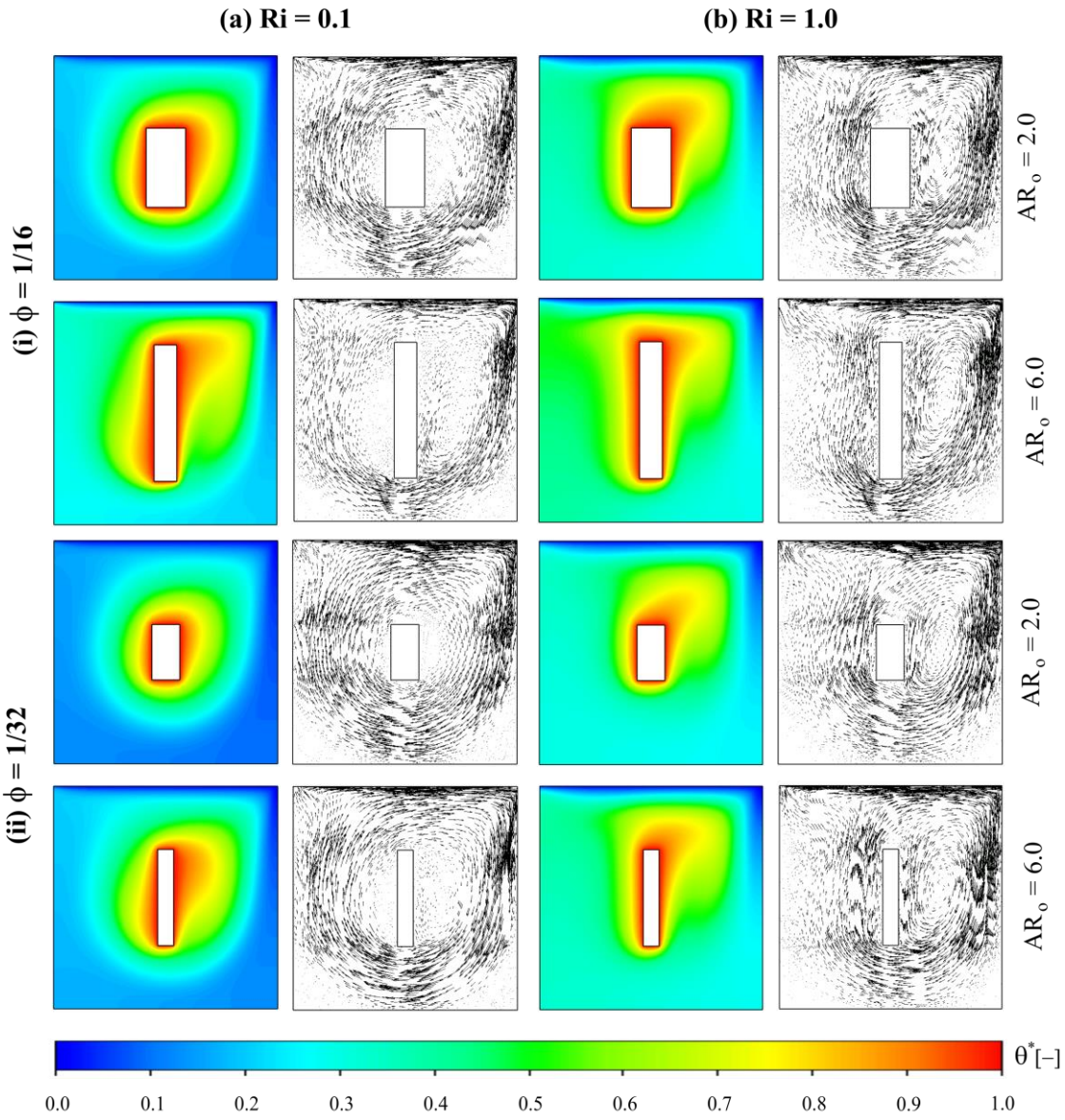

Figure 9 – θ^* fields and velocity vectors for AR_o = 2.0 and 6.0, where: (a) Ri = 0.1, (b) Ri = 1.0 and (i) ϕ = 1/16, (ii) ϕ = 1/32.

3.1 Effects of IB Horizontal Position

For the best geometric configuration (ϕ = 1/4 and AR_o = 3.0) in terms of q^*, a second DOF was admitted (IB horizontal position) after applying step 8 of the constructal design method (Fig. 2). Table 3 shows the q^* obtained in these cases with the HB center placed in different x_o^* (1/5, 1/4, 1/3, 2/3, 3/4, and 4/5) compared to the baseline geometry, where the IB is centered (x_o^* = 1/2) in the cavity.

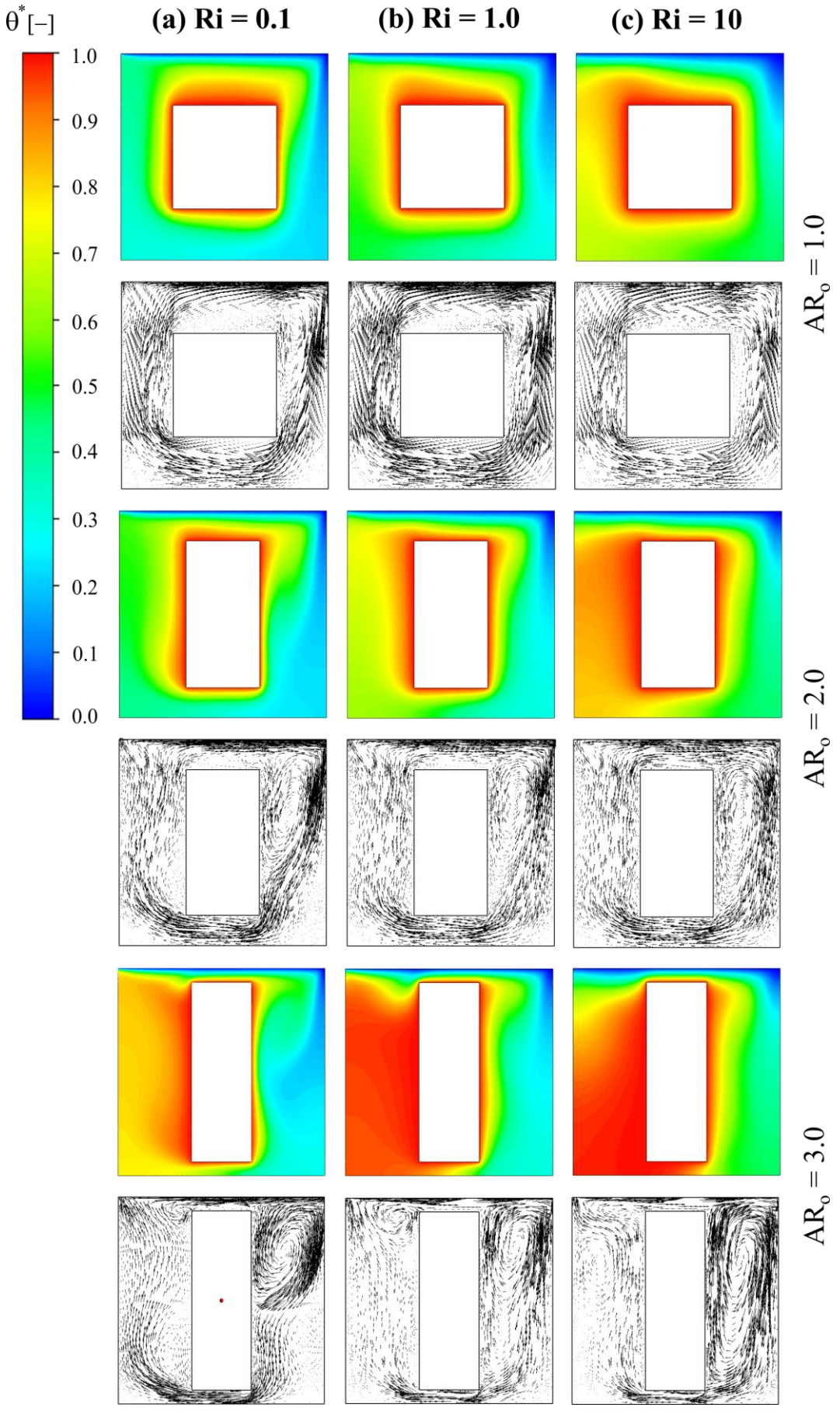

Figure 10 – θ^* fields and velocity vectors for ϕ = 1/4, where: (a) *Ri* = 0.1, (b) *Ri* = 1.0, (c) *Ri* = 10 and (i) AR_o = 1.0, (ii) AR_o = 2.0, (iii) AR_o = 3.0.

Table 3 – q^* obtained with ϕ = 1/4, AR_o = 3.0 and various *Ri* with the IB placed in different horizontal positions.

	Dimensionless Heat Rate (q^*)						
Ri	x_o^* = 1/5	x_o^* = 1/4	x_o^* = 1/3	x_o^* = 1/2	x_o^* = 2/3	x_o^* = 3/4	x_o^* = 4/5
0.1	15.47	18.91	19.51	19.18	19.14	**19.83**	17.11
1.0	11.87	13.04	13.50	**13.54**	12.78	11.47	10.06
10	10.09	10.43	**10.48**	9.81	8.60	8.16	7.90

As can be seen, q^* varies as a function of x_o^* differently for each *Ri*. When the forced convection is dominant (*Ri* = 0.1), q^*_{max} (19.83) is obtained with the IB center positioned slightly to the right (x_o^* = 3/4) of the cavity, while q^*_{max} (10.48) for *Ri* = 10 is obtained with the HB center placed to the left (x_o^* = 1/3). In percentage numbers, $q^*_{(x_o^*=3/4)}$ is 3.4% greater than $q^*_{(x_o^*=1/2)}$ for *Ri* = 0.1 and $q^*_{(x_o^*=1/3)}$ is 6.8% greater than $q^*_{(x_o^*=1/2)}$ for *Ri* = 10. On the other hand, q^*_{max} (13.54) related to the mixed convection cases (*Ri* = 1.0) is obtained with the baseline geometry, where the IB is centered in the cavity. This behavior indicates that the IB position influences the fluid flow differently for each convection regime, affecting the heat transfer as seen in Tab. 3. The role of IB position under the fluid flow can be better understood in Fig 11, where the θ^* fields and velocity vectors obtained with the IB center placed in different horizontal positions [x_o^* = (a) 1/4, (b) 1/3, (c) 1/2, (d) 2/3, and (e) 3/4] are presented for *Ri* = 0.1, 1.0 and 10.

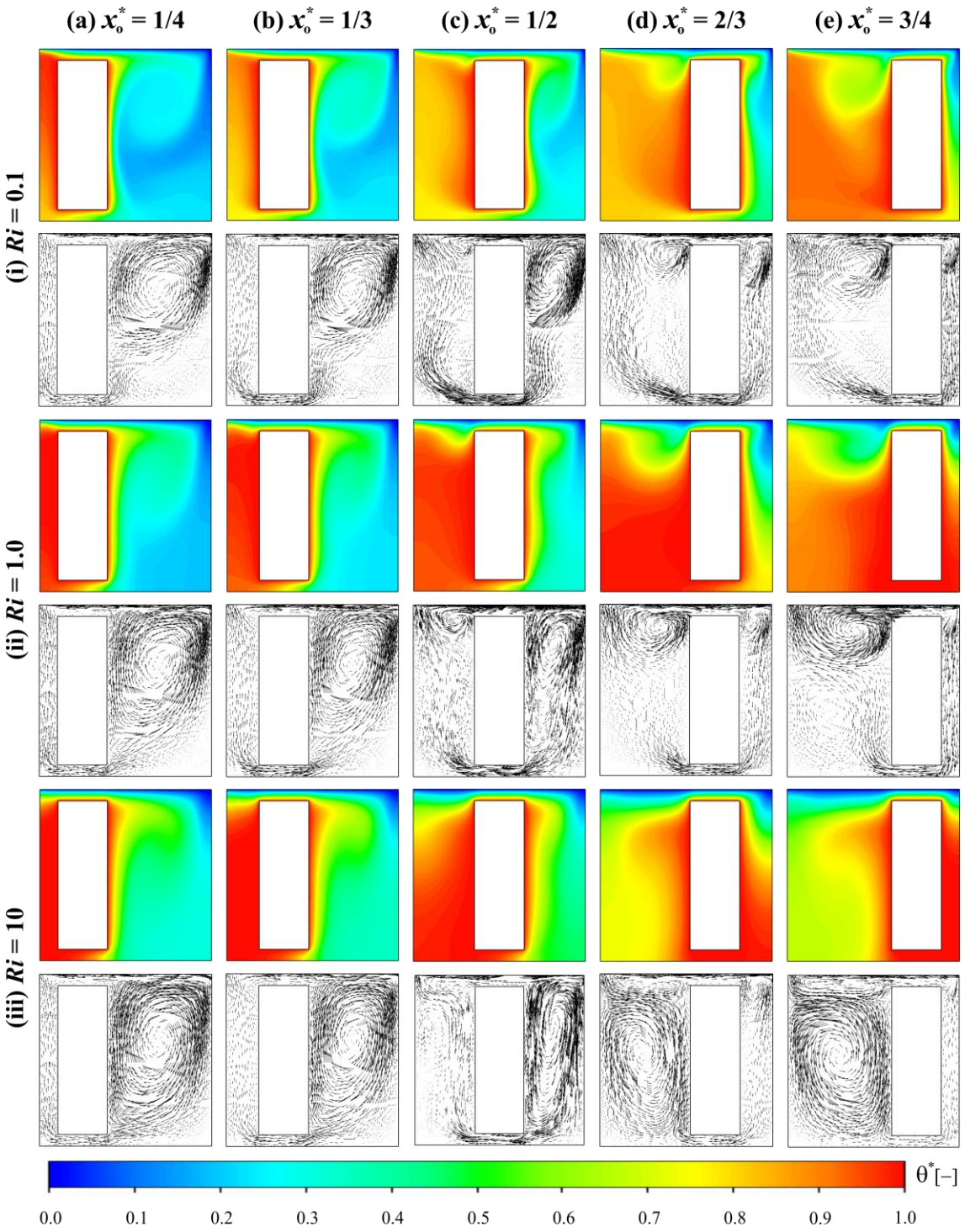

Figure 11 – θ^* fields and velocity vectors for $\phi = 1/4$ and various *Ri* with the IB positioned in different positions: (a) $x_o^* = 1/4$, (b) $x_o^* = 1/3$, (c) $x_o^* = 1/2$, (d) $x_o^* = 2/3$ and (e) $x_o^* = 3/4$.

Analyzing the velocity vectors presented in Fig. 11, a change in the fluid flow can be seen as the IB moves. For the natural convection cases (*Ri* = 10) with the IB placed on the left [Fig. 11 (iii) (a-b)], a large clockwise recirculation is observed in the right cavity region. However, this recirculation ends up divided into two counterclockwise cells when the IB is positioned to the right [Fig. 11 (iii) (d-e)]: one flat convective cell in the upper left cavity region and a main convective cell occupying the left remainder region. These

differences in the fluid flow explain the behavior observed for $q^*_{(Ri = 10)}$ in Tab. 3, where the highest q^* values were obtained with the IB on the left. When the IB is placed slightly to this side, there is an association of the ascendant flows generated by the natural convection and the lid movement. In these cases [Fig. 11 (iii) (a-b)], the ascending portion of the clockwise recirculation coincides with the fluid that ascends close to the IB due to the buoyant forces, which intensifies the convection and consequently the heat transfer. On the other hand, when the IB is positioned on the right [Fig. 11 (iii) (d-e)], the fluid that surpasses the inferior cavity channel and presents a tendency to ascend collides with the descending portion of the main counterclockwise recirculation. Furthermore, the portion of the fluid that manages to ascend is not satisfactorily cooled since the flat convective cell in the upper region ends up preventing the contact of the ascending fluid with the portion cooled by the moving wall, which is harmful to the heat transfer. The role played by the IB position in the fluid flow and heat transfer is also relevant for the forced convection cases (Ri = 0.1), where the q^*_{max} (19.83) was obtained with the IB positioned to the right (x_o^* = 3/4). In this case [Fig. 11 (i) (c)] no recirculation is formed in the right cavity channel, so the fluid that flows can descend more easily, without conflicting with any ascending hot parcel of fluid. This behavior is not observed for any other case with Ri = 0.1 [Fig. 11 (i) (a-d)], which confirms that the absence of flow conflicts is beneficial for the heat transfer since the highest q^* is associated with this case. Basically, the absence of flow conflicts in the right channel of the cavity allows the downward flow in that region to occur more intensely, promoting the heat transfer in that region.

4 CONCLUSIONS

Using the constructal design method, the main purpose of this numerical study was to maximize the dimensionless heat rate (q^*) in a lid-driven cavity with mixed convection and an isothermal block (IB) inside. The convective flow was considered two-dimensional, laminar, incompressible, and steady-state, while the working fluid is Newtonian. Conservative equations of mass, momentum, and energy are part of the mathematical model, which were solved using numerical simulations in ANSYS Fluent 2021 R1, a CFD code based on the finite volume method (FVM). For the problem geometry and fluid flow, one Degree of Freedom (DOF), IB aspect ratio ($0.5 \leq AR_o \leq 10$), and two parameters, Richardson Number (Ri = 0.1, 1.0, and 10) and the area fraction (ϕ = 1/4, 1/8, 1/16 and 1/32), were used to find the highest dimensionless heat rate (q^*)

between IB and cavity area. An additional DOF (IB horizontal position) was admitted to improve the best geometric configuration in terms of q^*. Considering many possible geometric and flow parameters, 162 configurations were analyzed for the lid-driven cavity with constant Grashof ($Gr = 10^5$) and Prandtl ($Pr = 0.71$). Among all numerical simulations carried out, the main findings were:

i. Along the horizontal cavity mid-plane ($H^* = 0.5$), right fluid positive v^* peaks indicate the occurrence of a contrary movement to the main flow that occurs in the negative direction, suggesting the existence of convective cells in the right cavity channel ($L^* > 0.5$). Velocity vectors confirm the existence of these convective cells, which take an elongated shape – even occupying the entire right cavity channel – as *Ri* increases in the higher AR_o cases.

ii. The heat transfer between the IB walls and the surrounding fluid flow is dependent on AR_o, *Ri*, and ϕ. Analyzing only *Ri*, the dimensionless heat rate (q^*) is maximized when the forced convection ($Ri = 0.1$) is dominant for $\phi = 1/4$ and $1/8$. For $\phi = 1/4$ and $AR_o = 3.0$, q^* obtained with $Ri = 0.1$ is 41.5% greater if compared to that obtained with $Ri = 1.0$ and 95.6% greater than that obtained with $Ri = 10$. However, this behavior only is valid for $\phi = 1/16$ when $AR_o > 4.0$, while for $\phi = 1/32$, the highest q^* is associated with the mixed convection ($Ri = 1.0$) cases.

iii. Regardless of *Ri*, the highest q^* is associated with the largest AR_o tested for each ϕ. For $\phi = 1/8$ and $Ri = 0.1$, q^* is 129.1% greater when AR_o increases from 1.0 to 6.0, while the most pronounced increase in q^* (143.2% greater) is observed for $\phi = 1/16$ and $Ri = 0.1$ when the HB assumes a tall shape ($AR_o = 10$) instead the square shape ($AR_o = 1.0$). This behavior can be explained by the IB perimeter that increases with AR_o, affecting the heat exchange area (A_{q^*}) when $AR_o > 1.0$. Therefore, A_{q^*} is larger for the highest AR_o cases, enhancing the heat transfer inside the cavity.

iv. Larger A_{q^*} also explains why q^* is maximized when $\phi = 1/4$ is adopted. In these cases, the larger is the IB size and its A_{q^*}, the higher is the heat transfer. Finally, the highest q^* (19.83) is obtained when the IB is positioned to the right ($x_o^* = 1/3$) with the following cavity and flow parameters: $\phi = 1/4$, $AR_o = 3.0$, and $Ri = 0.1$. Two factors can explain the greatest q^* observed for this configuration: the absence of relevant flow

circulations in the right cavity channel and the largest heat exchange area that enhances the heat transfer.

Thus, based on the results and the main findings, it can be concluded that the geometric parameters of the isothermal block inside the cavity played a relevant role in the fluid dynamic and thermal behavior of the investigated flow, as well as heat transfer performance. For practical applications, for example, the air cooling of electronic devices, the present results suggest that thermal control may be more effective if the device adopts a tall shape. For the flow, the most indicated is the use of velocities that guarantee the forced convection since it is through this convection regime that the highest dimensionless heat transfer rates were obtained. New degrees of freedom can be adopted for future studies, like the cavity aspect ratio and the vertical block position, as well as expanding the shapes and configurations studied in this paper, e.g., T-, Y-, and H-shaped of the blocks showing how the design change (evolution) can improve the performance of the system. In addition, higher lid velocities must be tested due to the turbulent flow may prove to be an effective way to potentiate the heat transfer between the isothermal obstacle and the surrounding fluid.

5 ACKNOWLEDGEMENTS

The authors acknowledge the agencies CAPES, CNPq, FAPERGS (Proc. No. 311444/2021-0) and the UNISINOS Academic Research and Postgraduate Unit. R.S. Borahel has a doctorate degree scholarship financed by CAPES (Code 001). F.S.F. Zinani is a grant holder of CNPq (Proc. No. 311444/2021-0). L.A.O. Rocha is a grant holder of CNPq (Proc. No. 307791/2019-0). Authors E.D. dos Santos and L.A. Isoldi thank CNPq for research grant (Proc. Nº 308396/2021-9, 309648/2021-1).

REFERENCES

[1] A. Bejan, The Physics of Life: The Evolution of Everything, St. Martin's Press, New York, 2016.

[2] A. Bejan, J.P. Zane, Design in Nature, Doubleday, New York, 2012.

[3] A. Bejan, S. Lorente, Design with Constructal Theory, John Wiley & Sons, Inc, New Jersey, 2008.

[4] A. Bejan, S. Lorente, The constructal law and the evolution of design in nature,

Phys. Life Rev. 8 (2011) 209–240. https://doi.org/10.1016/j.plrev.2011.05.010.

[5] E.D. Dos Santos, L.A. Isoldi, M.D.N. Gomes, L.A.O. Rocha, The Constructal Design Applied to Renewable Energy Systems, in: E. Ricón-Mejía, A. de las Heras (Eds.), Sustain. Energy Technol., CRC Press, Boca Raton, 2017: pp. 45–62.

[6] A. Bejan, Freedom and Evolution: Hierarchy in Nature, Society and Science, Springer, 2019.

[7] C.H. Lui, N.K. Fong, S. Lorente, A. Bejan, W.K. Chow, Constructal design for pedestrian movement in living spaces: Evacuation configurations, J. Appl. Phys. 111 (2012). https://doi.org/10.1063/1.3689771.

[8] C.H. Lui, N.K. Fong, S. Lorente, A. Bejan, W.K. Chow, Constructal design of evacuation from a three-dimensional living space, Physica A. 422 (2015) 47–57. https://doi.org/10.1016/j.physa.2014.12.005.

[9] A. Bejan, V. Badescu, A. De Vos, Constructal theory of economics structure generation in space and time, Energy Convers. Manag. 41 (2000) 1429–1451. https://doi.org/10.1016/S0196-8904(00)00038-8.

[10] A.H. Reis, Constructal view of scaling laws of river basins, Geomorphology. 78 (2006) 201–206. https://doi.org/10.1016/j.geomorph.2006.01.015.

[11] M. Reis, A. H.; Miguel, A. F.; Aydin, Constructal theory of flow architecture of the lungs, Med. Phys. 31 (2004) 1135–1140. https://doi.org/10.1118/1.1705443.

[12] R.F. Dutra, F.S.F. Zinani, L.A.O. Rocha, C. Biserni, Constructal design of an arterial bypass graft, Heat Transf. 49 (2020) 4019–4039. https://doi.org/10.1002/htj.21693.

[13] R.F. Dutra, F.S.F. Zinani, L.A.O. Rocha, C. Biserni, Effect of non-Newtonian fluid rheology on an arterial bypass graft: A numerical investigation guided by constructal design, Comput. Methods Programs Biomed. 201 (2021). https://doi.org/10.1016/j.cmpb.2021.105944.

[14] A.N. Impiombato, F.S.F. Zinani, L.A.O. Rocha, C. Biserni, Constructal Design Of An Idealize Arterial Bypass Graft: Effect Of The Bypass Attachment Pointon Resistance To Flow, J. Appl. Comput. Mech. 7 (2021) 334–344. https://doi.org/10.22055/jacm.2020.35246.2607.

[15] S. Lorente, E. Cetkin, T. Bello-Ochende, J.P. Meyer, A. Bejan, The constructal-law physics of why swimmers must spread their fingers and toes, J. Theor. Biol. 308 (2012) 141–146. https://doi.org/10.1016/j.jtbi.2012.05.033.

[16] A. Heitor Reis, Constructal view of the scaling laws of street networks - the dynamics behind geometry, Phys. A Stat. Mech. Its Appl. 387 (2008) 617–622.

https://doi.org/10.1016/j.physa.2007.10.003.

[17] P. Bieupoude, Y. Azoumah, P. Neveu, Optimization of drinking water distribution networks: Computer-based methods and constructal design, Comput. Environ. Urban Syst. 36 (2012) 434–444. https://doi.org/10.1016/j.compenvurbsys.2012.03.007.

[18] S. Lorente, A. Bejan, J.L. Niu, Constructal design of latent thermal energy storage with vertical spiral heaters, Int. J. Heat Mass Transf. 81 (2015) 283–288. https://doi.org/10.1016/j.ijheatmasstransfer.2014.09.077.

[19] V. Joshi, M.K. Rathod, Constructal enhancement of thermal transport in latent heat storage systems assisted with fins, Int. J. Therm. Sci. 145 (2019) 105984. https://doi.org/10.1016/j.ijthermalsci.2019.105984.

[20] A. Malley-Ernewein, S. Lorente, Constructal design of thermochemical energy storage, Int. J. Heat Mass Transf. 130 (2019) 1299–1306. https://doi.org/10.1016/j.ijheatmasstransfer.2018.10.097.

[21] M. Kepes Rodrigues, R. da Silva Brum, J. Vaz, L.A. Oliveira Rocha, E. Domingues dos Santos, L.A. Isoldi, Numerical investigation about the improvement of the thermal potential of an Earth-Air Heat Exchanger (EAHE) employing the Constructal Design method, Renew. Energy. 80 (2015) 538–551. https://doi.org/10.1016/j.renene.2015.02.041.

[22] R.J. Klein, C. Biserni, F.S.F. Zinani, L.A.O. Rocha, Constructal Design of tube arrangements for heat transfer to non-Newtonian fluids, Int. J. Mech. Sci. 133 (2017) 590–597. https://doi.org/10.1016/j.ijmecsci.2017.09.014.

[23] R.S. Brum, J.V.A. Ramalho, M.K. Rodrigues, L.A.O. Rocha, L.A. Isoldi, E.D. Dos Santos, Design evaluation of Earth-Air Heat Exchangers with multiple ducts, Renew. Energy. 135 (2019) 1371–1385. https://doi.org/10.1016/j.renene.2018.09.063.

[24] A.K. Barik, A. Mohanty, J.R. Senapati, M.M. Awad, Constructal design of different ribs for thermo-fluid performance enhancement of a solar air heater (SAH), Int. J. Therm. Sci. 160 (2021) 106655. https://doi.org/10.1016/j.ijthermalsci.2020.106655.

[25] G. Lorenzini, M.F.E. Lara, L.A.O. Rocha, M.D.N. Gomes, E.D. Dos Santos, L.A. Isoldi, Constructal design applied to the study of the geometry and submergence of an Oscillating Water Column, Int. J. Heat Technol. 33 (2015) 31–38. https://doi.org/10.18280/ijht.330205.

[26] R.S. Vieira, A.P. Petry, L.A.O. Rocha, L.A. Isoldi, E.D. dos Santos, Numerical

evaluation of a solar chimney geometry for different ground temperatures by means of constructal design, Renew. Energy. 109 (2017) 222–234. https://doi.org/10.1016/j.renene.2017.03.007.

[27] J.C. Martins, M.M. Goulart, M. das N. Gomes, J.A. Souza, L.A.O. Rocha, L.A. Isoldi, E.D. dos Santos, Geometric evaluation of the main operational principle of an overtopping wave energy converter by means of Constructal Design, Renew. Energy. 118 (2018) 727–741. https://doi.org/10.1016/j.renene.2017.11.061.

[28] A. Bejan interviewed by A. Kosner, "Freedom Is Good for Design," How to Use Constructal Theory to Liberate Any Flow System, Forbes. (2012). https://www.forbes.com/sites/anthonykosner/2012/03/18/freedom-is-good-for-design-how-to-use-constructal-theory-to-liberate-any-flow-system.

[29] L.A.O. Rocha, S. Lorente, A. Bejan, Constructal Theory in Heat Transfer, in: F.A. Kulacki (Ed.), Handb. Therm. Sci. Eng., Springer Cham, 2018.

[30] A.W. Islam, M.A.R. Sharif, E.S. Carlson, Mixed convection in a lid driven square cavity with an isothermally heated square blockage inside, Int. J. Heat Mass Transf. 55 (2012) 5244–5255. https://doi.org/10.1016/j.ijheatmasstransfer.2012.05.032.

[31] K.M. Gangawane, H.F. Oztop, N. Abu-Hamdeh, Mixed convection characteristic in a lid-driven cavity containing heated triangular block: Effect of location and size of block, Int. J. Heat Mass Transf. 124 (2018) 860–875. https://doi.org/10.1016/j.ijheatmasstransfer.2018.03.079.

[32] M. Manchanda, K.M. Gangawane, Mixed convection in a two-sided lid-driven cavity containing heated triangular block for non-Newtonian power-law fluids, Int. J. Mech. Sci. 144 (2018) 235–248. https://doi.org/10.1016/j.ijmecsci.2018.06.005.

[33] K.M. Gangawane, H.F. Oztop, M.E. Ali, Mixed convection in a lid-driven cavity containing triangular block with constant heat flux: Effect of location of block, Int. J. Mech. Sci. 152 (2019) 492–511. https://doi.org/10.1016/j.ijmecsci.2019.01.020.

[34] E.D. Dos Santos, G.L. Piccoli, F.H.R. França, A.P. Petry, Analysis of mixed convection in transient laminar and turbulent flows in driven cavities, Int. J. Heat Mass Transf. 54 (2011) 4585–4595. https://doi.org/10.1016/j.ijheatmasstransfer.2011.06.019.

[35] R. Iwatsu, J.M. Hyun, K. Kuwahara, Mixed convection in a driven cavity with a stable vertical temperature gradient, Int. J. Heat Mass Transf. 36 (1993) 1601–1608. https://doi.org/10.1016/S0017-9310(05)80069-9.

[36] P.M. Rodrigues, C. Biserni, C.C. de Escobar, L.A.O. Rocha, L.A. Isoldi, E.D. dos Santos, Geometric optimization of a lid-driven cavity with two rectangular

intrusions under mixed convection heat transfer: A numerical investigation motivated by constructal design, Int. Commun. Heat Mass Transf. 117 (2020) 104759. https://doi.org/10.1016/j.icheatmasstransfer.2020.104759.

[37] A.K. Prasad, J.R. Koseff, Combined forced and natural convection heat transfer in a deep lid-driven cavity flow, Int. J. Heat Fluid Flow. 17 (1996) 460–467. https://doi.org/10.1016/0142-727X(96)00054-9.

[38] K.N. Morshed, M.A.R. Sharif, A.W. Islam, Laminar Mixed Convection in a Lid-Driven Square Cavity with Two Isothermally Heated Square Internal Blockages, Chem. Eng. Commun. 202 (2015) 1176–1190. https://doi.org/10.1080/00986445.2014.912634.

[39] N. Nithyadevi, A. Shamadhani Begum, H.F. Oztop, N. Abu-Hamdeh, Mixed convection analysis in heat transfer enhancement of a nanofluid filled porous enclosure with various wall speed ratios, Int. J. Heat Mass Transf. 113 (2017) 716–729. https://doi.org/10.1016/j.ijheatmasstransfer.2017.05.134.

[40] A.K. Kareem, S. Gao, A.Q. Ahmed, Unsteady simulations of mixed convection heat transfer in a 3D closed lid-driven cavity, Int. J. Heat Mass Transf. 100 (2016) 121–130. https://doi.org/10.1016/j.ijheatmasstransfer.2016.04.073.

[41] R. Nimmagadda, R. Reuven, L.G. Asirvatham, S. Wongwises, Thermal Management of Electronic Devices Using Gold and Carbon Nanofluids in a Lid-Driven Square Cavity under the Effect of Variety of Magnetic Fields, IEEE Trans. Components, Packag. Manuf. Technol. 10 (2020) 1868–1878. https://doi.org/10.1109/TCPMT.2020.3008786.

[42] A.L. Razera, R.J.C. da Fonseca, L.A. Isoldi, E.D. dos Santos, L.A.O. Rocha, C. Biserni, Constructal design of a semi-elliptical fin inserted in a lid-driven square cavity with mixed convection, Int. J. Heat Mass Transf. 126 (2018) 81–94. https://doi.org/10.1016/j.ijheatmasstransfer.2018.05.157.

[43] H.F. Oztop, Z. Zhao, B. Yu, Fluid flow due to combined convection in lid-driven enclosure having a circular body, Int. J. Heat Fluid Flow. 30 (2009) 886–901. https://doi.org/10.1016/j.ijheatfluidflow.2009.04.009.

[44] K. Khanafer, S.M. Aithal, Mixed convection heat transfer in a lid-driven cavity with a rotating circular cylinder, Int. Commun. Heat Mass Transf. 86 (2017) 131–142. https://doi.org/10.1016/j.icheatmasstransfer.2017.05.025.

[45] A.K. Kareem, S. Gao, Mixed convection heat transfer of turbulent flow in a three-dimensional lid-driven cavity with a rotating cylinder, Int. J. Heat Mass Transf. 112 (2017) 185–200. https://doi.org/10.1016/j.ijheatmasstransfer.2017.04.118.

[46] F. Selimefendigil, H.F. Öztop, Numerical study of MHD mixed convection in a nanofluid filled lid driven square enclosure with a rotating cylinder, Int. J. Heat Mass Transf. 78 (2014) 741–754. https://doi.org/10.1016/j.ijheatmasstransfer.2014.07.031.

[47] A.K. Kareem, S. Gao, A comparison study of mixed convection heat transfer of turbulent nanofluid flow in a three-dimensional lid-driven enclosure with a clockwise versus an anticlockwise rotating cylinder, Int. Commun. Heat Mass Transf. 90 (2018) 44–55. https://doi.org/10.1016/j.icheatmasstransfer.2017.10.016.

[48] K.M. Gangawane, Computational analysis of mixed convection heat transfer characteristics in lid-driven cavity containing triangular block with constant heat flux: Effect of Prandtl and Grashof numbers, Int. J. Heat Mass Transf. 105 (2017) 34–57. https://doi.org/10.1016/j.ijheatmasstransfer.2016.09.061.

[49] K.M. Gangawane, B. Manikandan, Mixed convection characteristics in lid-driven cavity containing heated triangular block, Chinese J. Chem. Eng. 25 (2017) 1381–1394. https://doi.org/10.1016/j.cjche.2017.03.009.

[50] R. Nasrin, Aspect Ratio Effect of Vertical Lid Driven Chamber Having a Centered Conducting Solid on Mixed Magnetoconvection, J. Sci. Res. 3 (2011) 501–513. https://doi.org/10.3329/jsr.v3i3.7433.

[51] A.I. Alsabery, T. Tayebi, H.T. Kadhim, M. Ghalambaz, I. Hashim, A.J. Chamkha, Impact of two-phase hybrid nanofluid approach on mixed convection inside wavy lid-driven cavity having localized solid block, J. Adv. Res. 30 (2021) 63–74. https://doi.org/10.1016/j.jare.2020.09.008.

[52] W. Jamshed, M.R. Eid, S.M. Hussain, A. Abderrahmane, R. Safdar, O. Younis, A.A. Pasha, Physical specifications of MHD mixed convective of Ostwald-de Waele nanofluids in a vented-cavity with inner elliptic cylinder, Int. Commun. Heat Mass Transf. 134 (2022) 106038. https://doi.org/10.1016/j.icheatmasstransfer.2022.106038.

[53] S. Hussain, A.M. Aly, H.F. Öztop, Magneto-bioconvection flow of hybrid nanofluid in the presence of oxytactic bacteria in a lid-driven cavity with a streamlined obstacle, Int. Commun. Heat Mass Transf. 134 (2022). https://doi.org/10.1016/j.icheatmasstransfer.2022.106029.

[54] S. Ahmed, H. Xu, Y. Zhou, Q. Yu, Modelling convective transport of hybrid nanofluid in a lid driven square cavity with consideration of Brownian diffusion and thermophoresis, Int. Commun. Heat Mass Transf. 137 (2022) 106226.

https://doi.org/10.1016/j.icheatmasstransfer.2022.106226.

[55] M.A. Alomari, K. Al-Farhany, N.M. Said, M.A. Flayyih, Numerical investigation of double-diffusive mixed convection in a split lid-driven curvilinear cavity, Int. Commun. Heat Mass Transf. 138 (2022) 106322. https://doi.org/10.1016/j.icheatmasstransfer.2022.106322.

[56] Z. Korei, S. Benissaad, F. Berrahil, A. Filali, MHD mixed convection and irreversibility analysis of hybrid nanofluids in a partially heated lid-driven cavity chamfered from the bottom side, Int. Commun. Heat Mass Transf. 132 (2022) 105895. https://doi.org/10.1016/j.icheatmasstransfer.2022.105895.

[57] G. Lorenzini, B.S. Machado, L.A. Isoldi, E.D. Dos Santos, L.A.O. Rocha, Constructal design of rectangular fin intruded into mixed convective lid-driven cavity flows, J. Heat Transfer. 138 (2016) 1–12. https://doi.org/10.1115/1.4033378.

[58] A. Bejan, Convection Heat Transfer, 4th Ed, John Wiley & Sons, Inc, New Jersey, 2013.

[59] P.J. Roache, Verification and Validation in Computational Science and Engineering, Hermosa Publishers, Albuquerque, 1998.

[60] I.B. Celik, U. Ghia, P.J. Roache, C.J. Freitas, H. Coleman, P.E. Raad, Procedure for estimation and reporting of uncertainty due to discretization in CFD applications, J. Fluids Eng. Trans. ASME. 130 (2008) 0780011–0780014. https://doi.org/10.1115/1.2960953.

[61] N.O. Moraga, M.A. Marambio, R.C. Cabrales, Geometric multigrid technique for solving heat convection-diffusion and phase change problems, Int. Commun. Heat Mass Transf. 88 (2017) 108–119. https://doi.org/10.1016/j.icheatmasstransfer.2017.08.012.